In *Computational Photocatalysis: Modeling of Photophysics and Photochemistry at Interfaces;* ACS Symposium Series 1331; edited by Dmitri Kilin, Svetlana Kilina, and Yulun Han (American Chemical Society, Washington, 2019).

**Chapter 14**

# Photo-induced Charge Separation and Photoredox Catalysis in Cerium-Based Metal–Organic Frameworks

**Xin-Ping Wu and Donald G. Truhlar***

**Department of Chemistry, Chemical Theory Center, and Minnesota Supercomputing Institute, University of Minnesota, Minneapolis, Minnesota 55455-0431, United States**

***E-mail: truhlar@umn.edu**



Separation of photo-induced charges (electrons and holes) can exert important control over the lifetimes of photo-excited states. Such separation may be promoted in Metal–Organic frameworks (MOFs), which are organic–inorganic hybrid materials, through ligand-to-metal charge transfer (LMCT). In this chapter, we discuss our recent work on photocatalysis with Ce-based MOFs, which feature LMCT due to the low-lying empty 4f states of Ce(IV). We discuss the electronic structure of Ce-based UiO-66, the effects of linker functionalization and metal (Zr or Ti) doping on the electronic structure of Ce-based UiO-66, and the photoredox possibilities of the selected Ce-MOFs.

## Introduction

Photocatalysis provides a way to utilize sunlight and convert solar energy into chemical energy to meet the growing global demand for energy (*1–4*). This has led to the explosive growth in the past few decades in the study of photocatalysts, especially semiconductor-based photocatalysts (e.g., $d^0$, $d^{10}$, and $f^0$ metal oxides) featuring good stabilities, and in the study of the mechanism of photocatalysis (*4–14*). In case of semiconductor photocatalysis, the photocatalytic process involves three basic steps: (i) photo-induced excitation of the photocatalyst to generate charge carriers (electrons and holes), (ii) diffusion of charge carriers to the surface of the photocatalyst, and (iii) photoredox reactions on the photocatalyst surface (*7*).

Since the photoredox reactions are driven by the generated electrons and holes, the concentrations of these photo-induced charge carriers on the photocatalyst surface are crucial to the photocatalytic activity; larger or smaller amounts of surface charge carriers generally correspond to a higher or lower photocatalytic activity, respectively. An effective way to increase the concentrations of charge carriers on a photocatalyst surface is to suppress the recombination of charge carriers. If a longer diffusion pathway is required for the charge carriers to reach surface, it can result in a higher probability of recombination, giving rise to less charge carriers reaching the photocatalyst surface, and the probability for recombination can be decreased by making the particle size of a photocatalyst

smaller. Other approaches to suppress recombination include employing hybrid materials (e.g., heterojunction systems or organic–inorganic hybrid materials that are composed of two or more constituents) to separate the charge carriers spatially (*15*–*19*) and involving a cocatalyst (e.g., noble metal clusters) to trap the charge carriers (*20*, *21*).

Metal–Organic frameworks (MOFs) are hybrid materials, in particular porous crystalline materials with inorganometallic nodes connected into a polymeric network by organic linkers (*22*). One important feature of MOFs is that their porosity allows the rapid diffusion of reactants throughout the framework, and this provides an avenue to overcome the low mobility of charge carriers in many nonporous semiconductors. In addition, the small-scale nodes in MOFs behave similarly to quantum dots and have short diffusion pathways for charge carriers to reach the surface of a pore. Accordingly, MOFs intrinsically couple the characteristics of quantum dots and hybrid materials. With careful designs of the inorganic and organic building blocks (nodes and linkers), effective separation of charge carriers can be achieved during photocatalysis; successful cases include long-lived charge-separated states found in a zeolitic imidazolate framework ZIF-67 (*23*) and a trinuclear iron-$\mu_3$-oxo-based MOF MIL-100(Fe) (*24*).

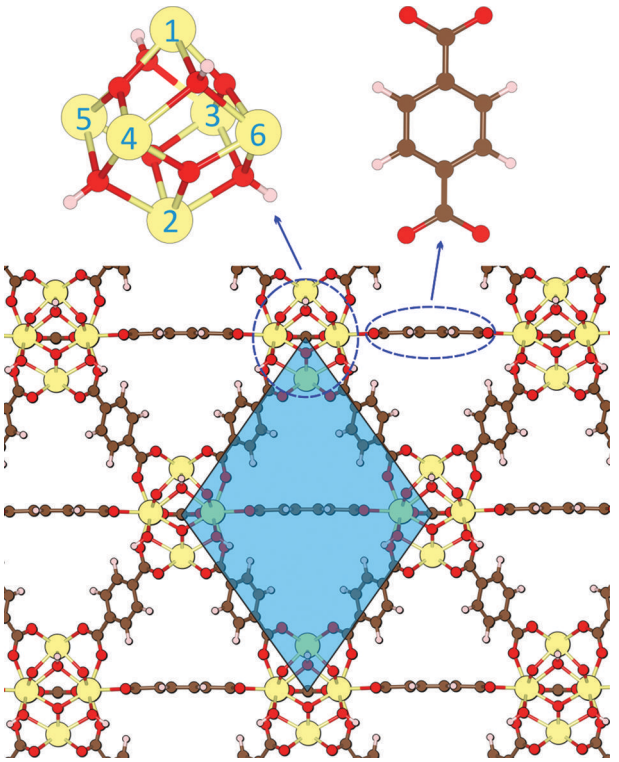


*Figure 1. Schematic view of pristine UiO-66. The primitive cell is indicated by a blue background. The six metal atoms are labeled with numbers and are identical for single-metal UiO-66 MOFs. Metal, H, C, and O atoms are in yellow, light pink, brown, and red, respectively. This color scheme is used throughout this chapter.*

Stability of photocatalysts in certain conditions (e.g., aqueous solution) is an essential requirement for practical applications (e.g., photocatalytic water splitting). However, MOFs generally have weak stability (*25*). Nevertheless, the UiO-66 MOF (see Figure 1), which is assembled by connecting $Zr_6(\mu_3\text{-}O)_4(\mu_3\text{-}OH)_4$ nodes and 1,4-benzene-dicarboxylate (BDC) linkers, achieved

a breakthrough in this respect (*26*); it has been reported that UiO-66 has exceptional thermal stability and strong resistance toward solvents (e.g., water) and pressure (*26*). Furthermore, UiO-66 has a broad tunability; (complete or partial) substitution of the Zr ions in the $Zr_6(\mu_3\text{-}O)_4(\mu_3\text{-}OH)_4$ node with Hf (*27*, *28*), Th (*29*), Ti (*28*), Ce (*30*), or U (*31*, *32*) and functionalization of the BDC linker with chemical groups (e.g., $NH_2$ or $NO_2$) (*33*, *34*) are synthetically feasible and can generate a series of UiO-66 analogs. Accordingly, photocatalysis on UiO-66 analogs has been studied for years (*28*, *35*–*45*). However, most of these studies focused on the original Zr-based UiO-66 with functionalized linkers responsible for light harvesting, and the ligand-to-metal charge transfer (LMCT) process, which can bring out the spatial separation of photo-induced charge carriers, is not favored in Zr-based UiO-66 (*42*, *44*), limiting the photocatalytic activity of Zr-based UiO-66 (*42*).

Our recent quantum mechanical computational work (*46*, *47*) shows that:

(i) By changing the $d^0$ metal Zr(IV) in the original Zr-based UiO-66 with the $f^0$ metal Ce(IV), the LMCT process becomes energetically favorable, and effective photo-induced charge separation may be achieved.
(ii) By functionalizing the BDC linker in Ce-based UiO-66, the light-harvesting capability of the BDC linker can be enhanced, and the electronic structure of Ce-based UiO-66 can be engineered for a desired reaction (e.g., photocatalytic water splitting).
(iii) By doping Ti or Zr in the Ce-based UiO-66, the electronic structure of Ce-based UiO-66 can be further optimized for photocatalytic reactions under visible light.

In this chapter, we will review this work.

## Computational Details

In this section, we give the details of calculations in the work (*46*, *47*) that is discussed in this chapter.

For clarity, we first introduce a notation UiO-66($M1_nM2_{6-n}$)-L to define the UiO-66 analogs, where M1 and M2 are the metals in the node, *n* is the number of M1 atoms in each node, and L denotes the functional group(s) (i.e., X or 2,5-X, see Figure 2) on the BDC linker. For single-metal UiO-66, the notation reduces to UiO-66($M_6$)-L, where M is the only metal in the node.

### Periodic Calculations

The unit cell of pristine UiO-66 consists of 456 atoms, and density functional theory (DFT) calculations on this cell would be very demanding. Therefore, to reduce the cost, we used the primitive cell of UiO-66 (see Figure 1), which consists of 114 atoms (6 metals, 32 O, 48 C, and 28 H) for the pristine structure.

All the periodic DFT calculations based on the primitive cell of UiO-66 were performed in the *Vienna ab initio Simulation Package* (*VASP*) (*48*, *49*). For all the periodic structures considered, both the atomic positions and the cell shape were optimized using the PBEsol (*50*) exchange–correlation functional because we found that PBEsol can give good equilibrium lattice constants for UiO-66($M_6$) (*46*). The optimizations were stopped when the Hellman–Feynman force on each relaxed ion was less than 0.02 eV/Å.

Previous work (*40*) showed that the HSE06 (*51*) exchange–correlation functional has useful accuracy for predicting band gaps of functionalized UiO-66($Zr_6$), and therefore it was selected to perform calculations of the density of states (DOS) of the PBEsol-optimized structures (this protocol is denoted as HSE06//PBEsol).

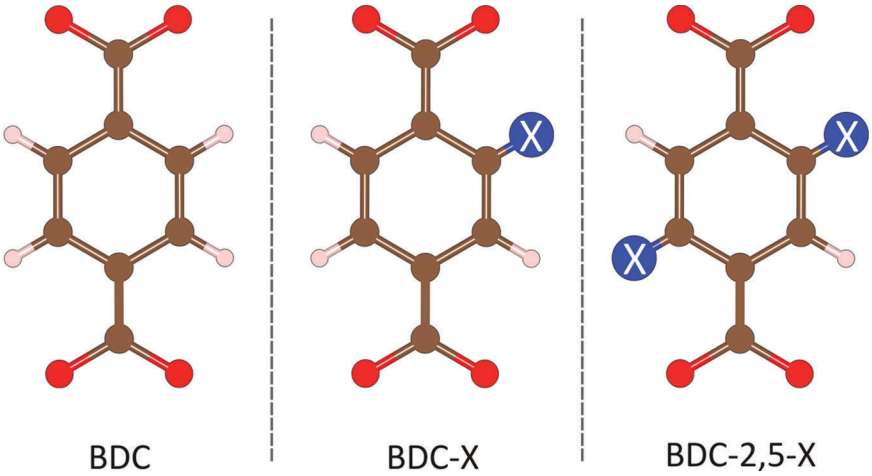


*Figure 2. BDC, BDC-X, and BDC-2,5-X linkers. The functionalized BDC linkers are discussed in the Linker Functionalization subsection in the Electronic Structure section.*

For all the periodic DFT calculations, the criterion for self-consistent field convergence was set at $10^{-5}$ eV, the kinetic energy cutoff was set at 500 eV, and the projector augmented wave (PAW) method (*52*) was used to describe the core–valence electron interactions with H (1s), C (2s, 2p), N (2s, 2p), O (2s, 2p), S (3s, 3p), F (2s, 2p), Cl (3s, 3p), Br (4s, 4p), I (5s, 5p), Ti (3s, 3p, 4s, 3d), Zr (4s, 4p, 5s, 4d), Hf (5s, 5p, 6s, 5d), Th (6s, 6p, 7s, 6d), Ce (5s, 5p, 6s, 5d, 4f), and U (6s, 6p, 7s, 5f, 6d) being treated as valence electrons.

For PBEsol optimization calculations, the *k*-point mesh was sampled using a 3 × 3 × 3 Monkhorst–Pack grid, while for HSE06 DOS calculations the 1 × 1 × 1 *k*-point mesh sampling (i.e., Γ-point sampling) was used to accelerate the computationally expensive HSE06 calculations since Γ-point sampling is expected to be adequate for calculating electronic properties (*40*, *42*).

**Cluster Calculations**

The isolated $H_2$BDC-X linkers with X = H, $NH_2$, $NO_2$, F, Cl, Br, I, OH, SH, COOH, $CH_3$, $CF_3$, or $SO_3H$ and the cluster model of the UiO-66($Ce_6$) used for excited-state calculations to obtain respective linker-localized excitations and node-localized and ligand-to-metal charge-transfer excitations were constructed by cutting the BDC-$X^{2-}$ and $[Ce_6O_4(OH)_4(BDC)_2(COO)_{10}]^{12-}$ anions from their optimized periodic systems UiO-66($Ce_6$)-X and capping the unsaturated sites with protons. The proton capping ions in these models were optimized to obtain ground-state structures. Vertical transitions were considered in excited-state calculations based on time-dependent density functional theory (TD-DFT) with the adiabatic linear-response approximation (*53*).

The HSE06 exchange–correlation functional with the 6-311+G(d) (*54*) basis set for H, C, N, O, S, F, Cl, and Br, the 6-311G(d) (*54*) basis set for I, and the Stuttgart–Dresden–Dunning (SDD, MWB28) (*55*) basis set and effective core potential for Ce was used for both the ground-state and

excited-state calculations on cluster models. All these cluster calculations were performed in *Gaussian 16* (*56*).

### Band Alignment

Butler and co-workers proposed a method to evaluate the vacuum levels of MOFs (*57*). They assumed that the common vacuum level of a MOF can be estimated by the electrostatic potential at the center of a pore of the MOF. In practice, the mean of the electrostatic potential values within a spherical probe, which is placed at the center of a pore of a MOF, is taken as the electrostatic reference potential, and to ensure that the obtained electrostatic reference potential is robust, the variance of the electrostatic potential values within the spherical probe should be very small.

We applied this method to the UiO-66 analogs to obtain their electrostatic reference potentials and derive their absolute band edge positions. We placed the spherical electrostatic probe (with a radius of 1 Å) at the center of the large octahedral cage (~11 Å) of each analog of UiO-66; the variance of the electrostatic potential values within the spherical probe was found to be lower than $10^{-4}$ V.

**Table 1. Transitions of Isolated $H_2$BDC-X Linkers (X = H, $NH_2$, $NO_2$, F, Cl, Br, I, OH, SH, COOH, $CH_3$, $CF_3$, or $SO_3H$) Dominated by HOLO → LULO Configurations**

| | *transition* | *excitation energy (eV)* | *oscillator strength, f* | *HOLO → LULO contribution (%)* |
|---|---|---|---|---|
| H | $S_0 \rightarrow S_3$ | 4.54 | 0.041 | 59 |
| $NH_2$ | $S_0 \rightarrow S_1$ | 3.41 | 0.096 | 97 |
| $NO_2$ | $S_0 \rightarrow S_5$ | 4.40 | 0.034 | 79 |
| F | $S_0 \rightarrow S_3$ | 4.39 | 0.047 | 90 |
| Cl | $S_0 \rightarrow S_2$ | 4.18 | 0.050 | 80 |
| Br | $S_0 \rightarrow S_1$ | 4.06 | 0.061 | 93 |
| I | $S_0 \rightarrow S_1$ | 3.76 | 0.063 | 96 |
| OH | $S_0 \rightarrow S_1$ | 3.80 | 0.088 | 96 |
| SH | $S_0 \rightarrow S_1$ | 3.40 | 0.075 | 97 |
| COOH | $S_0 \rightarrow S_1$ | 3.89 | 0.036 | 83 |
| $CH_3$ | $S_0 \rightarrow S_2$ | 4.32 | 0.031 | 59 |
| $CF_3$ | $S_0 \rightarrow S_3$ | 4.56 | 0.086 | 60 |
| $SO_3H$ | $S_0 \rightarrow S_2$ | 4.29 | 0.045 | 36 |

## Electronic Structure

Light absorption can generate excited states, and consequently the absorption spectrum is a key property of a photocatalyst. Typically, for MOF UiO-66($Zr_6$) and its functionalized variants, and many other MOFs, the linker is capable of light absorption (*40*, *42*, *44*, *58–60*), and the excitation

of the linker can be considered as the first step of the photocatalytic process in these MOFs. The absorption threshold is approximated by assuming that it corresponds to a transition from the highest occupied linker orbital (HOLO) to the lowest unoccupied linker orbital (LULO), and that the energy of this transition is given by

$$E_{abs} = E_{LULO} - E_{HOLO}, \quad (1)$$

where $E_{LULO}$ and $E_{HOLO}$ are the orbital energies. Using these orbitals is justified for the UiO-66 analogs by TD-DFT calculations on their isolated linkers ($H_2$BDC-X) that show that the transitions are dominated by HOLO → LULO configurations having large oscillator strengths (see Table 1).

The visible region of solar irradiance spans 1.7 to 3.2 eV and carries nearly half of the total solar energy that reaches the surface of the Earth. To absorb in the visible region, $E_{abs}$ should be lower than 3.2 eV, and to absorb a sufficient amount of solar light, it is desirable for $E_{abs}$ to be around 2 eV.

In photocatalysis, the lifetime of the excited states is of great importance as it needs to be long enough to drive the reaction. Effective separation of charge carriers can prolong the lifetime of the excited states, and for MOFs this can be achieved through the LMCT process (see Scheme 1). The rate of the LMCT process depends strongly on the electronic coupling strength and the nuclear reorganization of the involved vibronic states (*61*–*66*). Nevertheless, the energetic feasibility of the LMCT process can be estimated by $E_{LMCT}$, which is defined by

$$E_{LMCT} = E_{LUNO} - E_{LULO}, \quad (2)$$

where $E_{LUNO}$ is the energy of the lowest unoccupied node orbital (LUNO). Therefore, $E_{LMCT}$ corresponds to the energy change of transferring the photo-generated electron from the photo-excited linker orbital (which is assumed to be the LULO) to the LUNO.

It is desirable to have a negative $E_{LMCT}$, since it can favor the LMCT process and lead to long-lived LMCT excited state of the MOF photocatalyst (see Case 2 in Scheme 1). This requires the energy of the LUNO to be lower than the energy of the LULO.

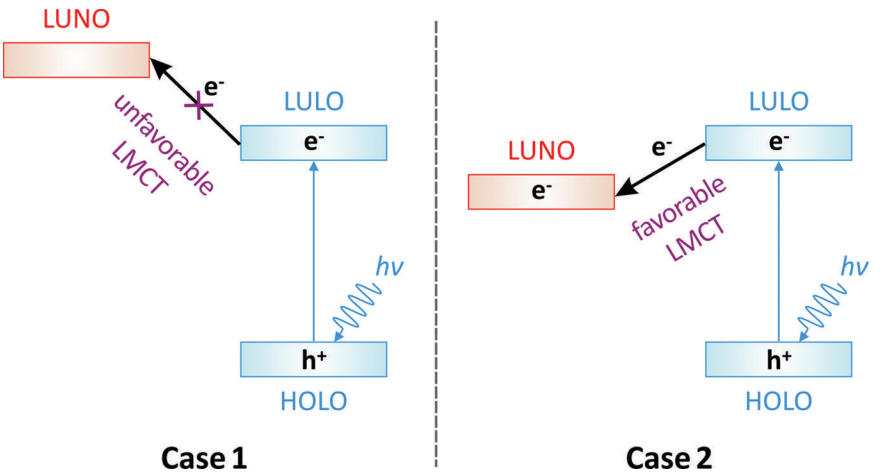


*Scheme 1. Two possible cases of LMCT processes in MOFs with photo-excited linker (note that MOF linkers are capable of harvesting light). HOLO, LULO, and LUNO represent highest occupied linker orbital, lowest unoccupied linker orbital, and lowest unoccupied node orbital, respectively.*

Both $E_{abs}$ and $E_{LMCT}$ are relevant to the photocatalytic activity of MOFs with light-harvesting linker (e.g., UiO-66 analogs). Accordingly, these two properties were taken as the descriptors to screen potential photocatalytic materials.

**Pristine UiO-66($M_6$)**

The left panel in Figure 3 illustrates the electronic structure of UiO-66($Zr_6$), and it shows that the highest occupied and lowest unoccupied crystal orbitals (HOCO and LUCO) are predominantly centered on the linkers, that is, the HOCO and the HOLO are the same for UiO-66($Zr_6$), and the LUCO is the same as the LULO. The calculated $E_{abs}$ for UiO-66($Zr_6$) is high (3.73 eV), indicating that pristine UiO-66($Zr_6$) does not absorb visible light.

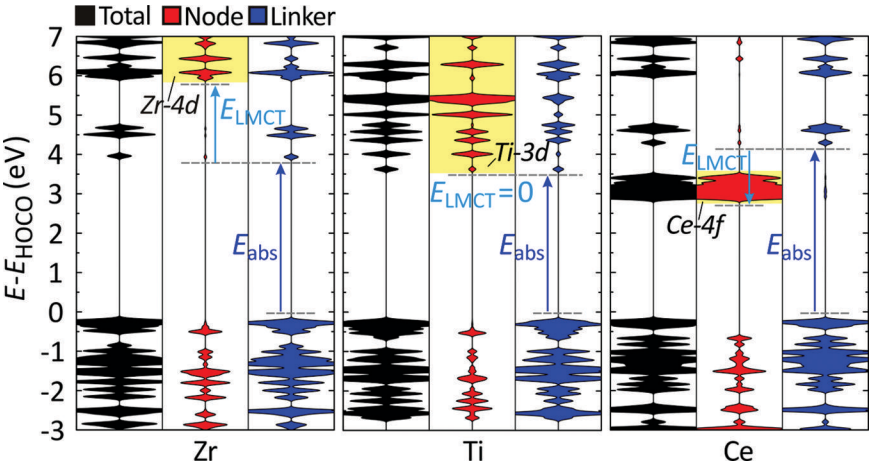


*Figure 3. Total (black) and projected (red and blue) density of states of the pristine UiO-66($M_6$) with M = Zr, Ti, or Ce. The unoccupied Zr 4d orbitals, Ti 3d orbitals, and Ce 4f orbitals are highlighted with a yellow background. The $E_{abs}$ and $E_{LMCT}$ for each case are labeled. $E_{HOCO}$ is the energy of the HOCO (i.e., HOLO for these three cases).*

The electronic structure of UiO-66($Zr_6$) also shows that the LUNO (which is a 4d orbital of Zr) is much higher in energy than the LULO (or LUCO). The calculated $E_{LMCT}$ for UiO-66($Zr_6$) is large and positive (2.00 eV), indicating that LMCT does not occur in this MOF, and the lifetime of excited states is expected to be short, which is consistent with the experimental observations by Nasalevich and co-workers (*42*). These results suggest that UiO-66($Zr_6$) has only limited photocatalytic activity.

To increase the photocatalytic activity of UiO-66($Zr_6$), both the $E_{abs}$ and the $E_{LMCT}$ need to be properly engineered. An effective approach to engineer the $E_{LMCT}$ of UiO-66($Zr_6$) is to replace the Zr with other metals (Hf, Th, Ti, Ce or U) since the LUNO, which can affect $E_{LMCT}$, is a metal orbital. We considered complete metal substitution of the $Zr_6(\mu_3\text{-}O)_4(\mu_3\text{-}OH)_4$ node with Hf, Th, Ti, Ce or U; these metals provide a variety of distinct valence orbitals (3d, 5d, 6d, 4f, and 5f).

The calculated $E_{abs}$ and $E_{LMCT}$ of the UiO-66($Zr_6$) and five analogs with other metals in place of Zr are tabulated in Table 2. Although Zr(IV), Hf(IV), Th(IV), and Ti(IV) are all $d^0$ metal ions, we find that UiO-66($Ti_6$) has very different electronic properties ($E_{abs}$ and $E_{LMCT}$) than UiO-66($M_6$) MOFs composed with M = Zr, Hf, or Th. The Zr, Hf, and Th MOFs are similar to each other but the

Ti MOF has much lower $E_{abs}$ and $E_{LMCT}$ (see Table 2). This is explained by the electronic structures of UiO-66($Zr_6$) and UiO-66($Ti_6$) in Figure 3; in particular, some 3d orbitals of Ti are found to be low in energy; this agrees with the fact that the $TiO_2$ 2p–3d band gap is much narrower than the $ZrO_2$ 2p–4d band gap (*65*–*67*), suggesting that one can design the electronic properties of UiO-66($M_6$) MOFs based on the knowledge of the corresponding metal dioxides. In addition, the energies of the 3d orbitals of Ti and the linker π* orbital are effectively overlapped, giving rise to a lower $E_{abs}$ in UiO-66($Ti_6$) than in UiO-66($Zr_6$). These results suggest that the photocatalytic activity and LMCT efficiency of UiO-66($Ti_6$) should be higher than that of UiO-66($Zr_6$), which is consistent with the experimental observations by Nasalevich and co-workers (*42*).

**Table 2. Absorption Energies ($E_{abs}$, in eV) and Ligand-to-Metal Charge-Transfer Energies ($E_{LMCT}$, in eV) of UiO-66($M_6$) with M = Zr, Hf, Th, Ti, Ce, or U**

| | *Zr* | *Hf* | *Th* | *Ti* | *Ce* | *U*[a] |
|---|---|---|---|---|---|---|
| $E_{abs}$ | 3.73 | 3.76 | 3.89 | 3.42 | 4.09 | 3.64 |
| $E_{LMCT}$ | 2.00 | 2.03 | 1.87 | 0 | -1.43 | 1.67 |

[a] UiO-66($U_6$) has six possible arrangements of magnetic spins, which have similar stabilities and electronic properties ($E_{abs}$ and $E_{LMCT}$). The data reported in this table adopts the most stable arrangement (i.e., the ferromagnetic state).

$CeO_2$, which features low-lying empty 4f orbitals, is highly reducible (*68*–*70*) and is often used as the catalytic support or even the catalyst for a wide range of redox reactions (*71*–*76*). It is reasonable to expect that the low-lying nature of the empty 4f orbitals in $CeO_2$ can be preserved in UiO-66($Ce_6$). In fact, our calculations show that UiO-66($Ce_6$) has a unique electronic structure (see Figure 3); the empty 4f band of UiO-66($Ce_6$) lies between the HOLO (or HOCO) and the LULO. Our TD-DFT calculations confirmed that node-localized excitations and ligand-to-metal charge-transfer excitations dominated by $2p_{C,O} \rightarrow 4f_{Ce}$ configurations are weak with oscillator strengths being generally close to or smaller than 0.001, confirming that the excitations are predominantly on the linker of UiO-66($Ce_6$). Therefore, UiO-66($Ce_6$) has a negative $E_{LMCT}$ (-1.43 eV, see Table 2), and the LMCT process, which can prevent the recombination of electrons and holes and generate long-lived charge-separated states, is energetically favorable in UiO-66($Ce_6$), with the low-lying empty 4f orbitals serving as efficient electron traps. Accordingly, UiO-66($Ce_6$) is promising for photocatalysis though it has a high $E_{abs}$ that must be lowered; this lowering will be addressed in the next two subsections.

Although U(IV), like Ce(IV), has empty f orbitals, UiO-66($U_6$) has a large and positive $E_{LMCT}$ (1.67 eV, see Table 2). The reason for this is that the unoccupied 5f orbitals of U are at high energies (*46*).

### Linker Functionalization

Linker functionalization has been found to be effective for enhancing the light-harvesting capability of MOFs (*40*, *58*). We therefore considered functionalizing UiO-66($Ce_6$) with 12

synthetically feasible monosubstituted variants of the BDC linker, i.e., BDC-X; see Figure 2. The substitutions we considered are X = $NH_2$, $NO_2$, F, Cl, Br, I, OH, SH, COOH, $CH_3$, $CF_3$, and $SO_3H$. Previous work indicated that $NH_2$ substitution might be especially effective, as the $NH_2$ group has been widely used to functionalize MOF linkers for enhancing their light-harvesting capabilities (*28*, *35*, *36*, *38*, *40–42*, *45*).

The calculated $E_{abs}$ and $E_{LMCT}$ of the resulting UiO-66($Ce_6$)-X MOFs are tabulated in Table 3. The table shows that the $E_{abs}$ (4.09 eV) of pristine UiO-66($Ce_6$) is more or less decreased after linker functionalization (*46*). Among the cases studied, the $E_{abs}$ of UiO-66($Ce_6$)-SH (2.54 eV) and UiO-66($Ce_6$)-$NH_2$ (2.74 eV) are decreased the most, indicating that functionalizing the linker with electron-donating SH or $NH_2$ groups is an effective way to decrease $E_{abs}$ and enhance the light-harvesting capability.

**Table 3. Absorption Energies ($E_{abs}$, in eV), Ligand-to-Metal Charge-Transfer Energies ($E_{LMCT}$, in eV), and HOCO–LUCO Gaps ($E_g$, in eV) of UiO-66($Ce_6$)-X and UiO-66($Ce_6$)-2,5-X**

| *X or 2,5-X* | $E_{abs}$ | $E_{LMCT}$ | $E_g$ |
|---|---|---|---|
| H | 4.09 | -1.43 | 2.66 |
| $NH_2$ | 2.74 | -1.57 | 1.17 |
| $NO_2$ | 3.77 | -1.33 | 2.44 |
| F | 3.83 | -1.38 | 2.45 |
| Cl | 3.57 | -1.39 | 2.18 |
| Br | 3.42 | -1.42 | 2.00 |
| I | 2.97 | -1.44 | 1.53 |
| OH | 3.02 | -1.61 | 1.41 |
| SH | 2.54 | -1.59 | 0.95 |
| COOH | 3.43 | -1.65 | 1.78 |
| $CH_3$ | 3.83 | -1.47 | 2.36 |
| $CF_3$ | 4.03 | -1.35 | 2.68 |
| $SO_3H$ | 3.70 | -1.50 | 2.20 |
| 2,5-$NH_2$ | 1.89 | -1.72 | 0.17 |
| 2,5-$NO_2$ | 3.19 | -1.06 | 2.13 |
| 2,5-Br | 3.16 | -1.44 | 1.72 |
| 2,5-I | 2.76 | -1.50 | 1.26 |
| 2,5-OH | 2.11 | -1.78 | 0.33 |
| 2,5-SH | 1.82 | -1.73 | 0.09 |

Previous study reported that the light-harvesting capability of the monosubstituted BDC linker can be further enhanced by difunctionalization (*40*). We then further considered six disubstituted

variants of BDC linker (i.e., BDC-2,5-X, see Figure 2), including BDC-2,5-$NH_2$, -2,5-$NO_2$, -2,5-Br, -2,5-I, -2,5-OH, and -2,5-SH; these functionalized linkers are suggested to have a similar or more superior light-harvesting capability than BDC-OH according to the simulated absorption spectra of isolated $H_2$BDC-X and $H_2$BDC-2,5-X linkers based on TD-DFT (*47*). The calculated $E_{abs}$ and $E_{LMCT}$ of the resulting UiO-66($Ce_6$)-2,5-X are also tabulated in Table 3. The results are consistent with the observation in a previous study (*40*); UiO-66($Ce_6$)-2,5-X has a lower $E_{abs}$ than the corresponding UiO-66($Ce_6$)-X.

## Metal Doping

In photocatalysis, metal-ion doping is a common and effective approach to optimize the photocatalyst (*12*, *77*, *78*). Inspired by this, we next studied mixed-metal UiO-66 MOFs.

Previous studies reported that it is feasible to dope Ti or Ce into the $Zr_6(\mu_3\text{-}O)_4(\mu_3\text{-}OH)_4$ node of UiO-66($Zr_6$) to form a mixed-metal (Ti/Zr or Ce/Zr) node (*28*, *79*–*85*). Our previous work suggested that the mixed Ce/Ti node, which has not been reported so far, can be synthesized since the energies of mixing Zr or Ti into the $Ce_6(\mu_3\text{-}O)_4(\mu_3\text{-}OH)_4$ node are comparable (*47*). Accordingly, we studied the effect of metal doping by considering mixed Ce/Zr and mixed Ce/Ti UiO-66 MOFs; more specifically, we considered the UiO-66($Ce_2Zr_4$) and UiO-66($Ce_2Ti_4$) MOFs for the reason that (i) for photocatalytic water splitting (note that in the next section we will focus on the photoredox possibility of the Ce-based MOFs for water splitting), two Ce sites holding excited electrons are sufficient to proceed the hydrogen evolution reaction (HER, $2H^+(aq) + 2e- \leftrightarrow H_2(g)$), which has much faster kinetics than the oxygen evolution reaction (OER, $H_2O \leftrightarrow 2H^+(aq) + 1/2O_2(g) + 2e-$) (*86*, *87*), and (ii) the effect of metal doping can be maximized.

**Table 4. Absorption Energies ($E_{abs}$, in eV), Ligand-to-Metal Charge-Transfer Energies ($E_{LMCT}$, in eV), and HOCO–LUCO Gaps ($E_g$, in eV) of UiO-66($Ce_2Zr_4$)-X, UiO-66($Ce_2Zr_4$)-2,5-X, UiO-66($Ce_2Ti_4$)-X, and UiO-66($Ce_2Ti_4$)-2,5-X**

| | *UiO-66($Ce_2Zr_4$)* | | | *UiO-66($Ce_2Ti_4$)* | | |
|---|---|---|---|---|---|---|
| ***X or 2,5-X*** | $E_{abs}$ | $E_{LMCT}$ | $E_g$ | $E_{abs}$ | $E_{LMCT}$ | $E_g$ |
| $NH_2$ | 2.48 | -1.11 | 1.37 | 2.14 | -0.92 | 1.22 |
| I | 2.76 | -0.99 | 1.76 | 2.55 | -0.90 | 1.65 |
| OH | 2.77 | -1.13 | 1.64 | 2.44 | -0.92 | 1.51 |
| SH | 2.37 | -1.09 | 1.27 | 2.04 | -0.92 | 1.12 |
| 2,5-$NH_2$ | 1.58 | -1.19 | 0.39 | 1.27 | -0.97 | 0.31 |
| 2,5-$NO_2$ | 3.02 | -0.67 | 2.35 | 2.93 | -0.63 | 2.30 |
| 2,5-Br | 2.95 | -0.98 | 1.97 | 2.66 | -0.83 | 1.83 |
| 2,5-I | 2.48 | -0.99 | 1.48 | 2.13 | -0.83 | 1.30 |
| 2,5-OH | 1.86 | -1.30 | 0.56 | 1.40 | -0.99 | 0.41 |
| 2,5-SH | 1.78 | -1.16 | 0.62 | 1.34 | -0.91 | 0.43 |

Both the UiO-66($Ce_2Zr_4$) and UiO-66($Ce_2Ti_4$) have their most stable doping configuration with the original Ce atoms at sites 1, 2, 3, and 5 (see Figure 1) in the UiO-66($Ce_6$) replaced by Zr or Ti (*47*). Such a doping configuration was adopted for further study. We considered 10 top-ranked functionalized linkers in Table 3 (i.e., BDC- $NH_2$, -I, -OH, -SH, -2,5-$NH_2$, -2,5-$NO_2$, -2,5-Br, -2,5-I, -2,5-OH, and -2,5-SH). The calculated $E_{abs}$ and $E_{LMCT}$, and HOCO–LUCO gaps ($E_g$) of the resulting MOFs are tabulated in Table 4. By comparing these results with the results in Table 3, we found that Zr or Ti doping can lower the $E_{abs}$ while opening the HOCO–LUCO gap and Ti doping is more effective in lowering the $E_{abs}$ than Zr doping. Therefore, we conclude that the electronic properties of Ce-MOFs can be further optimized by Zr or Ti doping.

## Photoredox Possibilities

Water splitting, which produces $H_2$ (which is clean energy source), is one of the most studied photocatalytic reactions (*3*, *88*–*90*). Therefore, water splitting was taken as the prototype reaction to screen the generated Ce-based MOF photocatalysts.

We first performed a preliminary screening on all generated Ce-based MOFs (listed in Tables 2 and 3) based on two criteria: (i) $E_{abs} \leq 3.0$ eV and (ii) $E_g \geq 1.48$ eV; the former criterion was used to screen visible-response photocatalysts and the latter criterion was used to satisfy the requirement of driving the water splitting reaction (HER and OER) using a single photocatalyst, that is, the lower limit of $E_g$ is 1.48 eV (1.23 + 0.25 eV) since the ideally minimal (HOCO–LUCO) gap to achieve water splitting is 1.23 eV and in practice an overpotential of 0.25 eV (*91*) or more (*3*) is required to drive water splitting. Nine Ce-based MOFs were then identified as candidates for visible-response water splitting photocatalysts: UiO-66($Ce_6$)-I, UiO-66($Ce_2Zr_4$)-L with L = 2,5-I, I, OH, and 2,5-Br, and UiO-66($Ce_2Ti_4$)-L with L = I, 2,5-$NO_2$, OH, and 2,5-Br. Among the nine candidates, eight MOFs (except the UiO-66($Ce_6$)-I) have a mixed-metal node, highlighting the significant effect of metal doping.

A further screening on the nine candidates considers their absolute band edge (HOCO and LUCO) positions (i.e., energies of HOCO and LUCO with respect to the vacuum level) since a qualified photocatalyst needs to have absolute band edges that can drive the photocatalytic reaction; for example, for the photocatalytic water splitting reaction, the absolute HOCO position of the MOF photocatalyst should be lower than the OER level while the absolute LUCO position of the MOF photocatalyst should be higher than the HER level. The condition that we considered for performing the photocatalytic water splitting reaction is room temperature (298.15 K) and pH = 7 (note that this is also a general condition for this reaction), and for this condition, the HER and OER levels are located at -3.87 and -5.09 eV, respectively (*46*).

The band alignment of the nine candidates at the condition considered is shown in Figure 4. It can be noticed that six Ce-based MOFs (i.e., UiO-66($Ce_6$)-I, UiO-66($Ce_2Zr_4$)-2,5-I, UiO-66($Ce_2Zr_4$)-I, UiO-66($Ce_2Zr_4$)-2,5-Br, UiO-66($Ce_2Ti_4$)-I, and UiO-66($Ce_2Ti_4$)-2,5-Br) generally have proper absolute HOCO and LUCO positions and were finally screened for potential visible-response water splitting photocatalysts. Among the six potential photocatalytic MOFs, the UiO-66($Ce_2Zr_4$)-2,5-I and UiO-66($Ce_2Ti_4$)-I are most promising as they have a low $E_{abs}$ of 2.48 and 2.55 eV, respectively, and thus have a great capability of light harvesting.

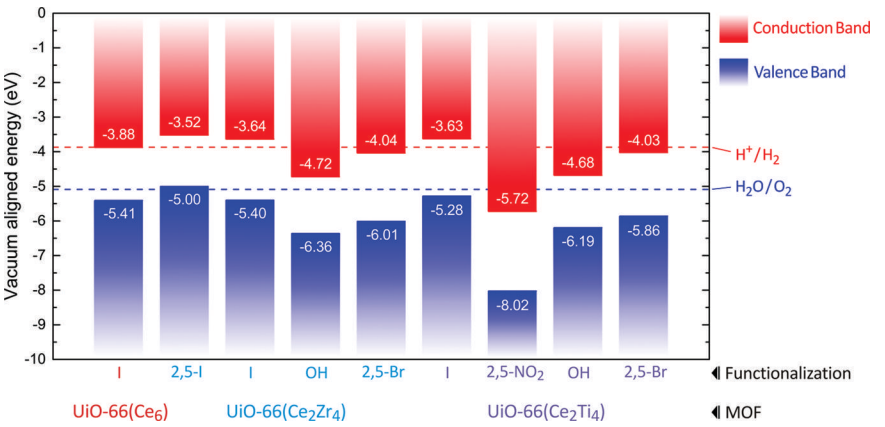


*Figure 4. Band alignment of UiO-66($Ce_6$)-I, UiO-66($Ce_2Zr_4$)-L with L = 2,5-I, I, OH, and 2,5-Br, and UiO-66($Ce_2Ti_4$)-L with L = I, 2,5-$NO_2$, OH, and 2,5-Br. For each case, the HOCO and the LUCO are on the functionalized linker and the Ce, respectively, and their vacuum aligned energies (white numbers) are given. The energies corresponding to the redox potentials for water splitting (at pH = 7 and T = 298.15 K) are represented by red and blue dashed lines.*

## Concluding Remarks

MOF photocatalysis is still at an early stage. Future directions in this research field include full utilization of the (organic–inorganic) hybrid nature of MOFs to develop photocatalytic MOFs that feature LMCT such that the lifetime of excited states can be prolonged in these MOFs.

In this respect, this chapter reviewed the (two) recent studies (*46*, *47*) on Ce-based MOF photocatalysts featuring LMCT. The main conclusions from these studies include:

(i) LMCT that can separate photo-induced charge carriers spatially and suppress their recombination in the MOF is energetically favorable in Ce-based MOFs due to the low-lying empty 4f states of Ce(IV).

(ii) Linker functionalization and metal doping are two effective approaches to enhance the light-harvest capability of a MOF photocatalyst and to engineer the electronic structure of a MOF photocatalyst for a desired reaction (e.g., water splitting).

(iii) For Ce-based UiO-66 MOFs, we proposed that UiO-66($Ce_6$)-I, UiO-66($Ce_2Zr_4$)-2,5-I, UiO-66($Ce_2Zr_4$)-I, UiO-66($Ce_2Zr_4$)-2,5-Br, UiO-66($Ce_2Ti_4$)-I, and UiO-66($Ce_2Ti_4$)-2,5-Br are potential visible-response water splitting photocatalysts, with UiO-66($Ce_2Zr_4$)-2,5-I and UiO-66($Ce_2Ti_4$)-I being most promising.

Future experimental studies on Ce-MOFs are needed to substantiate the findings based on theory. In addition, other linkers such as 4,4′-biphenyl-dicarboxylate (BPDC) in UiO-67 and terphenyl dicarboxylate (TPDC) in UiO-68 could be considered for combination with the Ce-based nodes (including the pure Ce node, the mixed Ce/Zr node, and the mixed Ce/Ti node) for future studies.

## Acknowledgments

The authors are grateful to Laura Gagliardi for collaboration. This research was supported as part of the Nanoporous Materials Genome Center by the U.S. Department of Energy, Office of Basic

Energy Sciences, Division of Chemical Sciences, Geosciences, and Biosciences, under Award No. DE-FG02-17ER16362.

## References


1. Gust, D.; Moore, T. A.; Moore, A. L. Solar Fuels via Artificial Photosynthesis. *Acc. Chem. Res.* **2009**, *42*, 1890–1898.
2. Barber, J. Photosynthetic Energy Conversion: Natural and Artificial. *Chem. Soc. Rev.* **2009**, *38*, 185–196.
3. Walter, M. G.; Warren, E. L.; McKone, J. R.; Boettcher, S. W.; Mi, Q.; Santori, E. A.; Lewis, N. S. Solar Water Splitting Cells. *Chem. Rev.* **2010**, *110*, 6446–6473.
4. Ismail, A. A.; Bahnemann, D. W. Photochemical Splitting of Water for Hydrogen Production by Photocatalysis: A Review. *Sol. Energy Mater. Sol. Cells.* **2014**, *128*, 85–101.
5. Fox, M. A.; Dulay, M. T. Heterogeneous Photocatalysis. *Chem. Rev.* **1993**, *93* (1), 341–357.
6. Hoffmann, M. R.; Martin, S. T.; Choi, W.; Bahnemann, D. W. Environmental Applications of Semiconductor Photocatalysis. *Chem. Rev.* **1995**, *95*, 69–96.
7. Mills, A.; Le Hunte, S. An Overview of Semiconductor Photocatalysis. *J. Photochem. Photobiol., A: Chem.* **1997**, *108*, 1–35.
8. Kudo, A.; Miseki, Y. Heterogeneous Photocatalyst Materials for Water Splitting. *Chem. Soc. Rev.* **2009**, *38*, 253–278.
9. Chen, X.; Shen, S.; Guo, L.; Mao, S. S. Semiconductor-based Photocatalytic Hydrogen Generation. *Chem. Rev.* **2010**, *110*, 6503–6570.
10. Serpone, N.; Emeline, A. V. Semiconductor Photocatalysis — Past, Present, and Future Outlook. *J. Phys. Chem. Lett.* **2012**, *3*, 673–677.
11. Nakata, K.; Fujishima, A. $TiO_2$ Photocatalysis: Design and Applications. *J. Photochem. Photobiol. C* **2012**, *13*, 169–189.
12. Schneider, J.; Matsuoka, M.; Takeuchi, M.; Zhang, J.; Horiuchi, Y.; Anpo, M.; Bahnemann, D. W. Understanding $TiO_2$ Photocatalysis: Mechanisms and Materials. *Chem. Rev.* **2014**, *114*, 9919–9986.
13. Hisatomi, T.; Kubota, J.; Domen, K. Recent Advances in Semiconductors for Photocatalytic and Photoelectrochemical Water Splitting. *Chem. Soc. Rev.* **2014**, *43*, 7520–7535.
14. Li, X.; Yu, J.; Jaroniec, M. Hierarchical Photocatalysts. *Chem. Soc. Rev.* **2016**, *45*, 2603–2636.
15. Vaynzof, Y.; Kabra, D.; Zhao, L.; Ho, P. K. H.; Wee, A. T.-S.; Friend, R. H. Improved Photoinduced Charge Carriers Separation in Organic-Inorganic Hybrid Photovoltaic Devices. *Appl. Phys. Lett.* **2010**, *97*, 033309.
16. Long, R.; English, N. J.; Prezhdo, O. V. Photo-induced Charge Separation across the Graphene–$TiO_2$ Interface Is Faster than Energy Losses: A Time-Domain *ab Initio* Analysis. *J. Am. Chem. Soc.* **2012**, *134*, 14238–14248.
17. Docampo, P.; Ball, J. M.; Darwich, M.; Eperon, G. E.; Snaith, H. J. Efficient Organometal Trihalide Perovskite Planar-Heterojunction Solar Cells on Flexible Polymer Substrates. *Nat. Commun.* **2013**, *4*, 2761.
18. Marschall, R. Semiconductor Composites: Strategies for Enhancing Charge Carrier Separation to Improve Photocatalytic Activity. *Adv. Funct. Mater.* **2014**, *24*, 2421–2440.

19. Wang, H.; Zhang, L.; Chen, Z.; Hu, J.; Li, S.; Wang, Z.; Liu, J.; Wang, X. Semiconductor Heterojunction Photocatalysts: Design, Construction, and Photocatalytic Performances. *Chem. Soc. Rev.* **2014**, *43*, 5234–5244.
20. Leathers, A. S.; Micha, D. A.; Kilin, D. S. Direct and Indirect Electron Transfer at A Semiconductor Surface with An Adsorbate: Theory and Application to $Ag_3Si(111)$:H. *J. Chem. Phys.* **2010**, *132*, 114702.
21. Yang, J.; Wang, D.; Han, H.; Li, C. Roles of Cocatalysts in Photocatalysis and Photoelectrocatalysis. *Acc. Chem. Res.* **2013**, *46*, 1900–1909.
22. Yaghi, O. M.; Li, H.; Davis, C.; Richardson, D.; Groy, T. L. Synthetic Strategies, Structure Patterns, and Emerging Properties in the Chemistry of Modular Porous Solids. *Acc. Chem. Res.* **1998**, *31*, 474–484.
23. Pattengale, B.; Yang, S.; Ludwig, J.; Huang, Z.; Zhang, X.; Huang, J. Exceptionally Long-Lived Charge Separated State in Zeolitic Imidazolate Framework: Implication for Photocatalytic Applications. *J. Am. Chem. Soc.* **2016**, *138*, 8072–8075.
24. Hanna, L.; Kucheryavy, P.; Liu, C.; Zhang, X.; Lockard, J. V. Long-Lived Photoinduced Charge Separation in a Trinuclear Iron-$\mu_3$-oxo-based Metal–Organic Framework. *J. Phys. Chem. C* **2017**, *121*, 13570–13576.
25. Férey, G. Hybrid Porous Solids: Past, Present, Future. *Chem. Soc. Rev.* **2008**, *37*, 191–214.
26. Cavka, J. H.; Jakobsen, S.; Olsbye, U.; Guillou, N.; Lamberti, C.; Bordiga, S.; Lillerud, K. P. A New Zirconium Inorganic Building Brick Forming Metal Organic Frameworks with Exceptional Stability. *J. Am. Chem. Soc.* **2008**, *130*, 13850–13851.
27. Jakobsen, S.; Gianolio, D.; Wragg, D. S.; Nilsen, M. H.; Emerich, H.; Bordiga, S.; Lamberti, C.; Olsbye, U.; Tilset, M.; Lillerud, K. P. Structural Determination of a Highly Stable Metal–Organic Framework with Possible Application to Interim Radioactive Waste Scavenging: Hf-UiO-66. *Phys. Rev. B: Condens. Matter Mater. Phys.* **2012**, *86*, 125429.
28. Yasin, A. S.; Li, J.; Wu, N.; Musho, T. Study of the Inorganic Substitution in A Functionalized UiO-66 Metal–Organic Framework. *Phys. Chem. Chem. Phys.* **2016**, *18*, 12748–12754.
29. Falaise, C.; Charles, J.-S.; Volkringer, C.; Loiseau, T. Thorium Terephthalates Coordination Polymers Synthesized in Solvothermal DMF/$H_2O$ System. *Inorg. Chem.* **2015**, *54*, 2235–2242.
30. Lammert, M.; Wharmby, M. T.; Smolders, S.; Bueken, B.; Lieb, A.; Lomachenko, K. A.; Vos, D. D.; Stock, N. Cerium-based Metal Organic Frameworks with UiO-66 Architecture: Synthesis, Properties and Redox Catalytic Activity. *Chem. Commun.* **2015**, *51*, 12578–12581.
31. Falaise, C.; Volkringer, C.; Vigier, J.-F.; Henry, N.; Beaurain, A.; Loiseau, T. Three-Dimensional MOF-Type Architectures with Tetravalent Uranium Hexanuclear Motifs ($U_6O_8$). *Chem.—Eur. J.* **2013**, *19*, 5324–5331.
32. Falaise, C.; Assen, A.; Mihalcea, I.; Volkringer, C.; Mesbah, A.; Dacheux, N.; Loiseau, T. Coordination Polymers of Uranium(IV) Terephthalates. *Dalton Trans.* **2015**, *44*, 2639–2649.
33. Hu, Z.; Zhao, D. *De facto* Methodologies Toward the Synthesis and Scale-up Production of UiO-66-Type Metal–Organic Frameworks and Membrane Materials. *Dalton Trans.* **2015**, *44*, 19018–19040.
34. Marshall, R. J.; Forgan, R. S. Postsynthetic Modification of Zirconium Metal–Organic Frameworks. *Eur. J. Inorg. Chem.* **2016**, *2016*, 4310–4331.

35. Gomes Silva, C.; Luz, I.; Llabrés i Xamena, F. X.; Corma, A.; García, H. Water Stable Zr-Benzenedicarboxylate Metal–Organic Frameworks as Photocatalysts for Hydrogen Generation. *Chem.—Eur. J.* **2010**, *16*, 11133–11138.
36. Sun, D.; Fu, Y.; Liu, W.; Ye, L.; Wang, D.; Yang, L.; Fu, X.; Li, Z. Studies on Photocatalytic $CO_2$ Reduction over $NH_2$-Uio-66(Zr) and Its Derivatives: Towards a Better Understanding of Photocatalysis on Metal–Organic Frameworks. *Chem.—Eur. J.* **2013**, *19*, 14279–14285.
37. Zhang, T.; Lin, W. Metal–Organic Frameworks for Artificial Photosynthesis and Photocatalysis. *Chem. Soc. Rev.* **2014**, *43*, 5982–5993.
38. Musho, T.; Li, J.; Wu, N. Band Gap Modulation of Functionalized Metal–Organic Frameworks. *Phys. Chem. Chem. Phys.* **2014**, *16*, 23646–23653.
39. Yang, L.-M.; Ganz, E.; Svelle, S.; Tilset, M. Computational Exploration of Newly Synthesized Zirconium Metal–Organic Frameworks UiO-66, -67, -68 and Analogues. *J. Mater. Chem. C* **2014**, *2*, 7111–7125.
40. Hendrickx, K.; Vanpoucke, D. E. P.; Leus, K.; Lejaeghere, K.; Van Yperen-De Deyne, A.; Van Speybroeck, V.; Van Der Voort, P.; Hemelsoet, K. Understanding Intrinsic Light Absorption Properties of UiO-66 Frameworks: A Combined Theoretical and Experimental Study. *Inorg. Chem.* **2015**, *54*, 10701–10710.
41. Otal, E. H.; Kim, M. L.; Calvo, M. E.; Karvonen, L.; Fabregas, I. O.; Sierra, C. A.; Hinestroza, J. P. A Panchromatic Modification of the Light Absorption Spectra of Metal–Organic Frameworks. *Chem. Commun.* **2016**, *52*, 6665–6668.
42. Nasalevich, M. A.; Hendon, C. H.; Santaclara, J. G.; Svane, K.; van der Linden, B.; Veber, S. L.; Fedin, M. V.; Houtepen, A. J.; van der Veen, M. A.; Kapteijn, F.; Walsh, A.; Gascon, J. Electronic Origins of Photocatalytic Activity in $d^0$ Metal Organic Frameworks. *Sci. Rep.* **2016**, *6*, 23676.
43. Yang, Z.; Xu, X.; Liang, X.; Lei, C.; Gao, L.; Hao, R.; Lu, D.; Lei, Z. Fabrication of Ce Doped UiO-66/Graphene Nanocomposites with Enhanced Visible Light Driven Photoactivity for Reduction of Nitroaromatic Compounds. *Appl. Surf. Sci.* **2017**, *420*, 276–285.
44. De Vos, A.; Hendrickx, K.; Van Der Voort, P.; Van Speybroeck, V.; Lejaeghere, K. Missing Linkers: An Alternative Pathway to UiO-66 Electronic Structure Engineering. *Chem. Mater.* **2017**, *29*, 3006–3019.
45. Santaclara, J. G.; Olivos-Suarez, A. I.; Gonzalez-Nelson, A.; Osadchii, D.; Nasalevich, M. A.; van der Veen, M. A.; Kapteijn, F.; Sheveleva, A. M.; Veber, S. L.; Fedin, M. V.; Murray, A. T.; Hendon, C. H.; Walsh, A.; Gascon, J. Revisiting the Incorporation of Ti(IV) in UiO-type Metal–Organic Frameworks: Metal Exchange versus Grafting and Their Implications on Photocatalysis. *Chem. Mater.* **2017**, *29*, 8963–8967.
46. Wu, X.-P.; Gagliardi, L.; Truhlar, D. G. Cerium Metal–Organic Framework for Photocatalysis. *J. Am. Chem. Soc.* **2018**, *140*, 7904–7912.
47. Wu, X.-P.; Gagliardi, L.; Truhlar, D. G. Metal Doping in Cerium Metal–Organic Frameworks for Visible-Response Water Splitting Photocatalysts. *J. Chem. Phys.* **2019**, *150*, 041701.
48. Kresse, G.; Hafner, J. *Ab Initio* Molecular-Dynamics Simulation of the Liquid-Metal–Amorphous-Semiconductor Transition in Germanium. *Phys. Rev. B: Condens. Matter Mater. Phys.* **1994**, *49*, 14251.

49. Kresse, G.; Furthmüller, J. Efficiency of Ab-Initio Total Energy Calculations for Metals and Semiconductors Using A Plane-Wave Basis Set. *Comput. Mater. Sci.* **1996**, *6*, 15.
50. Perdew, J. P.; Ruzsinszky, A.; Csonka, G. I.; Vydrov, O. A.; Scuseria, G. E.; Constantin, L. A.; Zhou, X.; Burke, K. Restoring the Density-Gradient Expansion for Exchange in Solids and Surfaces. *Phys. Rev. Lett.* **2008**, *100*, 136406.
51. Krukau, A. V.; Vydrov, O. A.; Izmaylov, A. F.; Scuseria, G. E. Influence of the Exchange Screening Parameter on the Performance of Screened Hybrid Functionals. *J. Chem. Phys.* **2006**, *125*, 224106.
52. Blöchl, P. E. Projector Augmented-Wave Method. *Phys. Rev. B: Condens. Matter Mater. Phys.* **1994**, *50*, 17953.
53. Casida, M. E.; Jamorski, C.; Casida, K. C.; Salahub, D. R. Molecular Excitation Energies to High-Lying Bound States from Time-Dependent Density-Functional Response Theory: Characterization and Correction of the Time-Dependent Local Density Approximation Ionization Threshold. *J. Chem. Phys.* **1998**, *108*, 4439–4449.
54. Hehre, W. J.; Random, L.; Schleyer, P. v. R.; Pople, J. A. *Ab Initio Molecular Orbital Theory*; Wiley: New York, 1986.
55. Dolg, M.; Stoll, H.; Preuss, H. Energy-Adjusted *Ab Initio* Pseudopotentials for the Rare Earth Elements. *J. Chem. Phys.* **1989**, *90*, 1730–1734.
56. Frisch, M. J.; Trucks, G. W.; Schlegel, H. B.; Scuseria, G. E.; Robb, M. A.; Cheeseman, J. R.; Scalmani, G.; Barone, V.; Petersson, G. A.; Nakatsuji, H.; Li, X.; Caricato, M.; Marenich, A. V.; Bloino, J.; Janesko, B. G.; Gomperts, R.; Mennucci, B.; Hratchian, H. P.; Ortiz, J. V.; Izmaylov, A. F.; Sonnenberg, J. L.; Williams; Ding, F.; Lipparini, F.; Egidi, F.; Goings, J.; Peng, B.; Petrone, A.; Henderson, T.; Ranasinghe, D.; Zakrzewski, V. G.; Gao, J.; Rega, N.; Zheng, G.; Liang, W.; Hada, M.; Ehara, M.; Toyota, K.; Fukuda, R.; Hasegawa, J.; Ishida, M.; Nakajima, T.; Honda, Y.; Kitao, O.; Nakai, H.; Vreven, T.; Throssell, K.; Montgomery, J. A., Jr.; Peralta, J. E.; Ogliaro, F.; Bearpark, M. J.; Heyd, J. J.; Brothers, E. N.; Kudin, K. N.; Staroverov, V. N.; Keith, T. A.; Kobayashi, R.; Normand, J.; Raghavachari, K.; Rendell, A. P.; Burant, J. C.; Iyengar, S. S.; Tomasi, J.; Cossi, M.; Millam, J. M.; Klene, M.; Adamo, C.; Cammi, R.; Ochterski, J. W.; Martin, R. L.; Morokuma, K.; Farkas, O.; Foresman, J. B.; Fox, D. J. *Gaussian 16*; Gaussian, Inc.: Wallingford, CT, 2016.
57. Butler, K. T.; Hendon, C. H.; Walsh, A. Electronic Chemical Potentials of Porous Metal–Organic Frameworks. *J. Am. Chem. Soc.* **2014**, *136*, 2703–2706.
58. Foster, M. E.; Azoulay, J. D.; Wong, B. M.; Allendorf, M. D. Novel Metal–Organic Framework Linkers for Light Harvesting Applications. *Chem. Sci.* **2014**, *5*, 2081–2090.
59. Dhakshinamoorthy, A.; Asiri, A. M.; García, H. Metal–Organic Framework (MOF) Compounds: Photocatalysts for Redox Reactions and Solar Fuel Production. *Angew. Chem., Int. Ed.* **2016**, *55*, 5414–5445.
60. Gutierrez, M.; Cohen, B.; Sánchez, F.; Douhal, A. Photochemistry of Zr-based MOFs: Ligand-to-Cluster Charge Transfer, Energy Transfer and Excimer Formation, What Else Is There? *Phys. Chem. Chem. Phys.* **2016**, *18*, 27761–27774.
61. Ulstrup, J.; Jortner, J. The Effect of Intramolecular Quantum Modes on Free Energy Relationships for Electron Transfer Reactions. *J. Chem. Phys.* **1975**, *63*, 4358–4368.

62. Siders, P.; Marcus, R. A. Quantum Effects in Electron-Transfer Reactions. *J. Am. Chem. Soc.* **1981**, *103*, 741–747.
63. Micha, D. A. Density Matrix Treatment of Non-Adiabatic Photoinduced Electron Transfer at A Semiconductor Surface. *J. Chem. Phys.* **2012**, *137*, 22A521.
64. Hembree, R. H.; Micha, D. A. Photoinduced Electron Transfer at A Si(111) Nanostructured Surface: Effect of Varying Light Wavelength, Temperature, and Structural Parameters. *J. Chem. Phys.* **2013**, *138*, 184708.
65. Miyazaki, S. Photoemission Study of Energy-Band Alignments and Gap-State Density Distributions for High-*k* Gate Dielectrics. *J. Vac. Sci. Technol. B* **2001**, *19*, 2212–2216.
66. Chen, X.; Mao, S. S. Titanium Dioxide Nanomaterials: Synthesis, Properties, Modifications, and Applications. *Chem. Rev.* **2007**, *107*, 2891–2959.
67. Bersch, E.; Rangan, S.; Bartynski, R. A.; Garfunkel, E.; Vescovo, E. Band Offsets of Ultrathin High-$\kappa$ Oxide Films with Si. *Phys. Rev. B* **2008**, *78*, 085114.
68. Esch, F.; Fabris, S.; Zhou, L.; Montini, T.; Africh, C.; Fornasiero, P.; Comelli, G.; Rosei, R. Electron Localization Determines Defect Formation on Ceria Substrates. *Science* **2005**, *309*, 752–755.
69. Jerratsch, J.-F.; Shao, X.; Nilius, N.; Freund, H.-J.; Popa, C.; Ganduglia-Pirovano, M. V.; Burow, A. M.; Sauer, J. Electron Localization in Defective Ceria Films: A Study with Scanning-Tunneling Microscopy and Density-Functional Theory. *Phys. Rev. Lett.* **2011**, *106*, 246801.
70. Wu, X.-P.; Gong, X.-Q. Clustering of Oxygen Vacancies at $CeO_2$(111): Critical Role of Hydroxyls. *Phys. Rev. Lett.* **2016**, *116*, 086102.
71. Paier, J.; Penschke, C.; Sauer, J. Oxygen Defects and Surface Chemistry of Ceria: Quantum Chemical Studies Compared to Experiment. *Chem. Rev.* **2013**, *113*, 3949–3985.
72. Wu, X.-P.; Gong, X.-Q. Unique Electronic and Structural Effects in Vanadia/Ceria-Catalyzed Reactions. *J. Am. Chem. Soc.* **2015**, *137*, 13228–13231.
73. Wu, X.-P.; Gong, X.-Q.; Lu, G. Role of Oxygen Vacancies in the Surface Evolution of H at $CeO_2$(111): A Charge Modification Effect. *Phys. Chem. Chem. Phys.* **2015**, *17*, 3544–3549.
74. Wu, X.-P.; Liu, J.; Fan, J.; Gong, X.-Q. Theoretical Studies on the Monomeric Vanadium Oxides Supported by Ceria: the Atomic Structures and Oxidative Dehydrogenation Activities. *RSC Adv.* **2015**, *5*, 52259–52263.
75. Montini, T.; Melchionna, M.; Monai, M.; Fornasiero, P. Fundamentals and Catalytic Applications of $CeO_2$-Based Materials. *Chem. Rev.* **2016**, *116*, 5987–6041.
76. Rodriguez, J. A.; Grinter, D. C.; Liu, Z.; Palominoa, R. M.; Senanayake, S. D. Ceria-based Model Catalysts: Fundamental Studies on the Importance of the Cetal–Ceria Interface in CO Oxidation, the Water–Gas Shift, $CO_2$ Hydrogenation, and Methane and Alcohol Reforming. *Chem. Soc. Rev.* **2017**, *46*, 1824–1841.
77. Ravelli, D.; Dondi, D.; Fagnoni, M.; Albini, A. Photocatalysis. A Multi-Faceted Concept for Green Chemistry. *Chem. Soc. Rev.* **2009**, *38*, 1999–2011.
78. Choi, J.; Park, H.; Hoffmann, M. R. Effects of Single Metal-Ion Doping on the Visible-Light Photoreactivity of $TiO_2$. *J. Phys. Chem. C* **2010**, *114*, 783–792.
79. Sun, D.; Liu, W.; Qiu, M.; Zhang, Y.; Li, Z. Introduction of A Mediator for Enhancing Photocatalytic Performance *via* Post-Synthetic Metal Exchange in Metal–Organic Frameworks (MOFs). *Chem. Commun.* **2015**, *51*, 2056–2059.

80. Lee, Y.; Kim, S.; Kang, J. K.; Cohen, S. M. Photocatalytic $CO_2$ Reduction by A Mixed Metal (Zr/Ti), Mixed Ligand Metal–Organic Framework under Visible Light Irradiation. *Chem. Commun.* **2015**, *51*, 5735–5738.
81. Nouar, F.; Breeze, M. I.; Campo, B. C.; Vimont, A.; Clet, G.; Daturi, M.; Devic, T.; Walton, R. I.; Serre, C. Tuning the Properties of the UiO-66 Metal Organic Framework by Ce Substitution. *Chem. Commun.* **2015**, *51*, 14458–14461.
82. Wang, A.; Zhou, Y.; Wang, Z.; Chen, M.; Sun, L.; Liu, X. Titanium Incorporated with UiO-66(Zr)-Type Metal–Organic Framework (MOF) for Photocatalytic Application. *RSC Adv.* **2016**, *6*, 3671–3679.
83. Tu, J.; Zeng, X.; Xu, F.; Wu, X.; Tian, Y.; Hou, X.; Long, Z. Microwave-induced Fast Incorporation of Titanium into UiO-66 Metal–Organic Frameworks for Enhanced Photocatalytic Properties. *Chem. Commun.* **2017**, *53*, 3361–3364.
84. Lammert, M.; Glißmann, C.; Stock, N. Tuning the Stability of Bimetallic Ce(IV)/Zr(IV)-based MOFs with UiO-66 and MOF-808 Structures. *Dalton Trans.* **2017**, *46*, 2425–2429.
85. Portillo, A. S.; Baldoví, H. G.; Fernandez, M. T. G.; Navalón, S.; Atienzar, P.; Ferrer, B.; Alvaro, M.; Garcia, H.; Li, Z. Ti as Mediator in the Photoinduced Electron Transfer of Mixed-Metal $NH_2$-UiO-66(Zr/Ti): Transient Absorption Spectroscopy Study and Application in Photovoltaic Cell. *J. Phys. Chem. C* **2017**, *121*, 7015–7024.
86. Nozik, A. J. Photoelectrolysis of Water Using Semiconducting $TiO_2$ Crystals. *Nature* **1975**, *257*, 383–386.
87. Dare-Edwards, M. P.; Goodenough, J. B.; Hamnett, A.; Trevellick, P. R. Electrochemistry and Photoelectrochemistry of Iron(III) Oxide. *J. Chem. Soc., Faraday Trans. 1* **1983**, *79*, 2027–2041.
88. Maeda, K.; Domen, K. Photocatalytic Water Splitting: Recent Progress and Future Challenges. *J. Phys. Chem. Lett.* **2010**, *1*, 2655–2661.
89. Acar, C.; Dincer, I.; Naterer, G. F. Review of Photocatalytic Water-Splitting Methods for Sustainable Hydrogen Production. *Int. J. Energy Res.* **2016**, *40*, 1449–1473.
90. Jafari, T.; Moharreri, E.; Amin, A. S.; Miao, R.; Song, W.; Suib, S. L. Photocatalytic Water Splitting—The Untamed Dream: A Review of Recent Advances. *Molecules* **2016**, *21*, 900.
91. Wrighton, M. S.; Ginley, D. S.; Wolczanski, P. T.; Ellis, A. B.; Morse, D. L.; Linz, A. Photoassisted Electrolysis of Water by Irradiation of A Titanium Dioxide Electrode. *Proc. Natl. Acad. Sci. U. S. A.* **1975**, *72*, 1518–1522.